

TARGET POROSITY CONTROLS CRATER RESIDUAL BOUGUER ANOMALY IN THE LUNAR HIGHLANDS. M. Ding¹, J. M. Soderblom¹, M. T. Zuber¹, C. J. Bierson², F. Nimmo², and C. Milbury³.
¹Department of Earth, Atmospheric and Planetary Sciences, Massachusetts Institute of Technology, Cambridge, MA 02139 (dingmin@mit.edu); ²Department of Earth and Planetary Sciences, University of California, Santa Cruz, CA 95064; ³Department of Earth, Atmospheric, and Planetary Sciences, Purdue University, West Lafayette, IN 47907.

Introduction: The high quality and resolution of the measures of the lunar gravity field provided by the Gravity Recovery and Interior Laboratory (GRAIL) mission and lunar topography by the Lunar Orbiter Laser Altimeter (LOLA) aboard the Lunar Reconnaissance Orbiter (LRO) provide an unprecedented opportunity to study the influence of impact cratering on the evolution of lunar crustal structure. Using these data we identify a positive correlation between crater residual Bouguer anomaly (RBA, defined as the mean Bouguer anomaly inside the crater rim, minus that of the local surroundings) and the regional porosity, for craters in the highlands [1]. The positive correlation is explained by numerical models [2], in which the processes of pore space generation and compaction by impact drives the crustal porosity to steady state. The steady state in porosity is estimated to be ~7% for lunar craters [2]. Here, we test for spatial correlation between crater RBA and target porosity.

Spatial Interpolation of Crater RBA: We selected craters with diameters from 20 to 100 km identified in LOLA topography [3; 4], yielding 4864 craters. We used GRAIL free-air gravity model JGGRAIL_1200C12A [5], filtered to include degrees 33 to 600 and subtracted the gravitational attraction of topography to derive the Bouguer anomaly, assuming a crustal density of 2,550 kg/m³ [6]. Following [1], we derived the crater RBA, and then used these RBA values to construct a global map on a 73×37 grid with a grid distance of 5°. Four spatial interpolation methods [7] were used to derive the spatial distribution.

Natural Neighbor Interpolation. This deterministic method first divides the data space into Voronoi polygons, each assigned the value of the corresponding control point. For any interpolating grid point, a new Voronoi polygon is created and the proportion of the overlap between the new polygon and the initial polygons is used as weighting for the interpolation.

Inverse Distance Weighted Interpolation. In this deterministic method, the weights are given by the inverse of the distance from the interpolating grid point to control points. Here we used a threshold cap radius of 10° to improve the speed of the interpolation.

Kriging. The geostatistical interpolation (*i.e.*, Kriging) takes advantage of spatial autocorrelation to objectively determine the distance-dependent weighting functions following the theory of probability

[8]. For each interpolating grid point, we first solved for local exponential variogram in 10° radius window, and then derived corresponding weights for each control point for a best unbiased local prediction. Kriging has the advantage of both preserving the local pattern and taking into account spatial autocorrelation.

Abel-Poisson Spline Interpolation. Spatial spline interpolation solves the coefficients for chosen spline functions that minimize the misfits between the observed and interpolated values at the control points. We utilized Abel-Poisson functions that are bandlimited in both spatial and spectral domains [9; 10]. The parameter h determines the spatial and spectral bandwidths of the Abel-Poisson functions. Our chosen value of 0.1 ensured consistency with our other techniques.

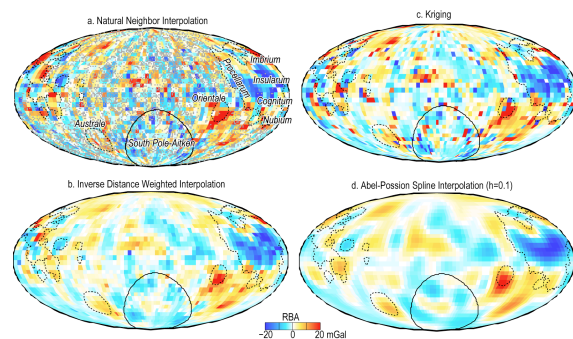


Figure 1. Interpolated RBA maps using four different methods, centered at 180°E, 0°N, on Mollweide equal area projection. The dashed lines contour the nearside mare regions, while the solid line indicates the SP-A basin.

The four interpolated RBA maps (Fig. 1) show a consistent spatial pattern at regional scales, though Natural Neighbor interpolation and Kriging preserve more local patterns. The spatial resolution of the maps was chosen to be 10° to match the resolution of the regional porosity model we considered later [11]. Significant negative RBA is found over most maria (contoured by dashed lines), including Oceanus Procellarum, Mare Imbrium, Mare Insularum, and Mare Cognitum.

The spatial variations in the crater RBA can result from variations in the (pre-impact) target porosity, impact processes, and post-impact surface infill. In

order to estimate the crater RBA caused by post-impact surface infill, we subtracted the observed crater floor depth from the expected fresh crater depth, $d = 1.044D_c^{0.301}$ [12] and constructed a global map using Inverse Distance Weighted interpolation. The maximum surface infill thickness was estimated to be ~ 2 km, corresponding to a RBA of about -5 mGal, assuming a breccia infill density of $2,490 \text{ kg/m}^3$ for the highlands [13]. This 5 mGal is too small to control the crater RBA variations in the range of ± 20 mGal. We therefore attribute the majority of the crater RBA variations in the highlands to target porosity. The situation is more complex for the maria, as the surface infill could also include mare basalt. Assuming a mare basalt density of $2,720 \text{ kg/m}^3$ [13], the addition to the RBA for 2 -km thick mare basalt will be ~ 14 mGal. This might be responsible for large positive RBA observed in some mare regions, e.g., the Mare Orientale and Mare Australe (Fig. 1).

We will consider the influence of target porosity later by utilizing the numerical results of [2]. We will assume that the crater diameter difference is caused by impactor diameter, as in [2], ignoring the possible difference in impact velocity, impact angle, and others. We will not take into account the detailed layering structure under the crater floor, including the fallback breccia and melt sheet, noticing that their total induced RBA is expected to be less than 5 mGal as the low-density breccia and high-density melt sheet will effectively compensate each other.

Target-Porosity-Controlled Crater RBA: Numerical simulations for impact processes [2] suggest that the crater RBA depends primarily on target porosity, and less on crater diameter. The numerical results were linearly interpolated and extrapolated to infer crater RBA values, yielding the relationship .

We calculated the target porosity as $\phi = 1 - \rho_b / \rho_0$, where ρ_b is averaged bulk density based on the depth-dependent exponential density model in [11] and ρ_0 is grain density in [14]. For each crater, ρ_b was calculated as the averaged bulk density within the depth column of an H_ϕ -thick underlying region with crater-induced porosity change, which we assume is related to the crater diameter D_c by a constant ratio. For a given value of H_ϕ/D_c , we calculated the target porosities and then inferred RBA values for the craters using the numerical results of [2]. The ratio H_ϕ/D_c was tested from 0 to 2.0 and a best-fit value of 1.0 was found to minimize the misfits between the inferred and observed crater RBA. Fig. 2 shows the interpolated maps for the averaged target porosity values at the crater locations and inferred RBA using Inverse Distance Weighted method.

The expected RBA (Fig. 2b) in the highlands generally has three distinct regions: a negative area in the northern hemisphere, a positive area near the equator and extending northwest, and a negative area in the SP-A basin [15]. The three long-wavelength structures also exist in the previous interpolated RBA maps (e.g., Fig. 1d). However, smaller-size spatial patterns in the interpolated RBA map, e.g., the positive RBA at the center of the SP-A basin, might indicate local porosity variation that cannot be resolved in the gravity admittance study of [11]. This confirms our expectation that crater gravity signals can act as probes into the underlying crustal structure.

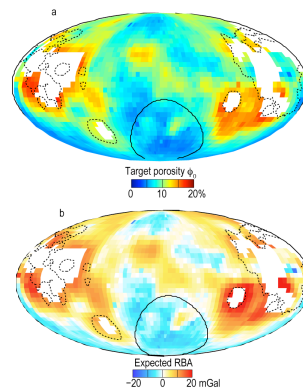


Figure 2. (a) Target porosity averaged within the depth column H_ϕ using the regional porosity model in [11]. (b) Expected RBA using the numerical simulation results in [2].

Conclusions: Based on the comparison between the crater RBA and the regional porosity, we conclude that the large-scale spatial variations in crater RBA can be explained by variations in regional porosity. Local variations in the crater RBA may indicate small-scale target porosity differences that were not resolved in the gravity admittance analysis of [11].

References: [1] Soderblom J. M. *et al.* (2015) *GRL*, 42, doi:10.1002/2015GL065022. [2] Milbury C. *et al.* (2015) *GRL*, 42, doi:10.1002/2015GL066198. [3] Head J. W. *et al.* (2010) *Science*, 329, doi:10.1126/science.1195050. [4] Kadish S. J. *et al.* (2011) *LPS XLII*, Abstract #1006. [5] Goosseens S. J. *et al.* (2015) *LPS XLVI* Abstract #1395. [6] Wieczorek M. A. *et al.* (2013) *Science*, 339, doi:10.1126/science.1231530. [7] Robeson S. M. (1997) *CGIS*, 24, 3-20. [8] Hengl T. (2009) *University of Amsterdam*, 291. [9] Amirbekyan A. *et al.* (2008) *GJI*, 174, doi:10.1111/j.1365-246X.2008.03809.x. [10] Freedon W. (1984) *JCAM*, 11, 367-375. [11] Besserer J. *et al.* (2014) *GRL*, 41, doi:10.1002/2014GL060240. [12] Melosh H. J. (1989) *Oxford University Press*, 245. [13] Kiefer W. S. *et al.* (2015) *LPS XLVI* Abstract #1711. [14] Huang Q. and Wieczorek M. A. (2012) *JGR*, 117, doi:10.1029/2012JE004062. [15] Phillips R. J. *et al.* (2015) *LPS XLVI* Abstract #2897.